Geophysical Journal International

Geophys. J. Int. (2016) **207,** 1783–1795
Advance Access publication 2016 October 5
GJI Geomagnetism, rock magnetism and palaeomagnetism

doi: 10.1093/gji/ggw376

Low-temperature magnetic properties of monoclinic pyrrhotite with particular relevance to the Besnus transition

Michael W.R. Volk,[1] Stuart A. Gilder[1] and Joshua M. Feinberg[2]

[1]*Department for Earth and Environmental Sciences, Ludwig Maximilians Universität, D-80333 München, Germany. E-mail:* *volk@geophysik.uni-muenchen.de*
[2]*Institute for Rock Magnetism, Department of Earth Sciences, University of Minnesota, Minneapolis, MN 55455, USA*

Accepted 2016 October 4. Received 2016 September 26; in original form 2016 July 29; Editorial Decision 2016 September 30

SUMMARY

Monoclinic pyrrhotite (Fe_7S_8) owes its ferrimagnetism to an ordered array of Fe vacancies. Its magnetic properties change markedly around 30 K, in what is known as the Besnus transition. Plausible explanations for the Besnus transition are either due to changes in crystalline anisotropy from a transformation in crystal symmetry or from the establishment of a two-phase system with magnetic interaction between the two phases. To help resolve this discrepancy, we measured hysteresis loops every 5° and backfield curves every 10° in the basal plane of an oriented single crystal of monoclinic pyrrhotite at 300 K and every 2 K from 50 K through the Besnus transition until 20 K. Between 50 and 30 K, hysteresis loops possess double inflections between crystallographic *a*-axes and only a single inflection parallel to the *a*-axes. Magnetization energy calculations and relative differences of the loops show a sixfold symmetry in this temperature range. We propose that the inflections stem from magnetic axis switching, which is both field and temperature dependent, in a manner somewhat analogous to an isotropic point where magnetocrystalline constants change their sign. The Besnus transition is best characterized by changes in magnetic remanence and coercivity over a 6° temperature span (28–34 K) with a maximum rate of change at 30 K. A surprising yet puzzling finding is that the coercivity ratio becomes less than unity below the transition when fourfold symmetry arises. Because the changes in magnetic parameters are linked to the crystal structure, we conclude the Besnus transition owes its origin to a distortion of the crystallographic axes below 30 K rather than an apparition of a two-phase system. An isothermal magnetization of natural pyrrhotite cycled from room temperature to successively lower temperatures through the Besnus transition decreases 2–4 times less than equivalent grain sizes of magnetite, with less than a 10 per cent loss in remanence between 300 and 150 K in pseudo-single-domain (PSD) pyrrhotite. As PSD monoclinic pyrrhotite carries the magnetic remanence in some meteorites, it is likely that low-temperature cycling in space then warming to ambient conditions at the Earth's surface will have only a minor influence on palaeointensity values derived from those meteorites.

Key words: Magnetic and electrical properties; Magnetic mineralogy and petrology; Palaeointensity; Rock and mineral magnetism; Phase transitions.

1 INTRODUCTION

Pyrrhotite refers to a group of non-stoichiometric iron sulfides, $Fe_{1-x}S$ with $0.08 < x < 0.125$, that are important carriers of magnetic remanence in some terrestrial and extraterrestrial rocks. The mineral group has a hexagonal (NiAs type) crystal structure consisting of alternating Fe and S layers. A slight distortion (β from 90° to ≈90.4°) of the crystal lattice in Fe_7S_8 lowers the symmetry from hexagonal to monoclinic, so it is commonly referred to as pseudo-hexagonal (Martin-Hernandez *et al.* 2008). Vacancies in the Fe layers lead to different superstructures (Morimoto *et al.* 1970), with the most iron deficient pyrrhotite (4C) having alternating layers of completely filled Fe sites and layers containing ordered vacancies at an Fe site (Bertaut 1953). Sublattice moments couple ferromagnetically within the basal plane while adjacent Fe layers couple antiferromagnetically. Regular ordering of vacancies in the basal plane and unequal sublattice moments gives rise to ferrimagnetism in monoclinic pyrrhotite (Néel 1952; Bertaut 1953; O'Reilly 1984). Hexagonal pyrrhotite ($Fe_{11}S_{12}$–Fe_9S_{10}) has equal but opposite sublattice moments at room temperature. Around 250 °C, hexagonal pyrrhotite undergoes the so-called lambda transition characterized by a reordering of the vacancy structure that transforms the crystal into a ferrimagnetic monoclinic form with a sharp increase in magnetization (Schwarz & Vaughan 1972). Monoclinic pyrrhotite has a Curie temperature of 320 °C and exhibits no lambda transition.

Vacancy ordering produces a strong magnetocrystalline anisotropy in Fe_7S_8 (Mikami *et al.* 1959; Bin & Pauthenet 1963; Sato *et al.* 1964; Martin-Hernandez *et al.* 2008). At room temperature, the hard magnetic axis parallels the *c*-axis, while the easy axis direction resides within the basal plane (Bin & Pauthenet 1963; Kind *et al.* 2013; Feinberg *et al.* 2015). Magnetic-domain observations mainly show 180° domain walls (Halgedahl & Fuller 1981; Soffel 1981). The multidomain (MD) threshold occurs at grain sizes >100 µm, while particles smaller than 2 µm are single domain (SD; Soffel 1977; Bezaeva *et al.* 2016); most magnetic parameters show grain size dependencies (Dekkers 1988, 1989; Menyeh & O'Reilly 1997).

Monoclinic pyrrhotite undergoes a magnetic phase transition around 30–34 K, called the Besnus transition (T_{Bes}) (Besnus & Meyer 1964; Fillion & Rochette 1988; Dekkers *et al.* 1989). When cooled in zero field, the transition is marked by a sudden loss of remanent magnetization as well as changes in other magnetic parameters (Dekkers *et al.* 1989; Kind *et al.* 2013; Koulialias *et al.* 2016). Why the transition occurs is debated. Some workers propose a crystallographic transformation from monoclinic to triclinic (Fillion & Rochette 1988; Rochette *et al.* 2011; Wolfers *et al.* 2011), while others argue for a reorientation of domain structure due to interacting superstructures independent of the 4C superstructure (Kind *et al.* 2013; Charilaou *et al.* 2015; Koulialias *et al.* 2016). To help elucidate this problem, we studied magnetic hysteresis and backfield curves on a single crystal of monoclinic (Fe_7S_8) pyrrhotite in 72 discrete angles at 22 discrete temperatures above, during and below T_{Bes}.

Another reason to study magnetic properties of monoclinic pyrrhotite at low temperatures is that it constitutes a major magnetic mineral in certain types of achondritic meteorites, including Martian meteorites, that potentially carries a record of the ancient magnetic fields on those bodies (Rochette *et al.* 2001, 2008; Weiss *et al.* 2002, 2008; Gattacceca & Rochette 2004). A largely unexplored problem is how low-temperature cycling in space influences the remanent magnetization of pyrrhotite, which may in turn bias the interpretation of palaeointensity data. Weiss *et al.* (2009) estimated the equilibrium temperature of a rotating meteorite at a distance of 3.5 AU to be ≈150–130 K. Thus, we question how temperature cycling will affect palaeointensity estimates if a extraterrestrial rock obtained a thermal remanent magnetization by cooling through the Curie temperature down to an equilibrium temperature of ≈150 K then subsequently arrived on the Earth's surface and warmed to ≈300 K. Dunlop (2003) carried out low-temperature cycling experiments on nine size fractions of magnetite (Fe_3O_4) where it was found that the amount of demagnetization strongly depends on particle size. We followed this example by studying the low-temperature cycling of natural pyrrhotite bearing rocks with different magnetic-domain states to assess the potential implications for meteorites.

2 MATERIALS, METHODS AND RESULTS

2.1 Samples

The Munich Mineralogical State Collection (Mineralogische Staatssammlung München) provided us with a single crystal of monoclinic pyrrhotite (sample MSM17591) to study the Besnus transition. It yielded a Curie temperature of 318 °C (Petersen Instruments, variable field translation balance, University of Munich) with no trace of a lambda transition. We drilled a disc from the single crystal measuring 2.6 mm in diameter and 0.75 mm in height—paying close attention that the disc was as circular as possible.

A JEOL 6500 field emission gun outfitted with an HKL electron backscatter diffraction (EBSD) detector (University of Minnesota) determined the sample's crystallography using an operating voltage of 20 kV and a working distance of 14.8 mm. Diffraction patterns were indexed using Channel 5 software with a monoclinic crystal structure described by Tokonami *et al.* (1972) and Powell *et al.* (2004). Crystallographic solutions were accepted only if the mean angular deviation value was less than 1.4°. Measurements of elemental abundances were collected using an accelerating voltage of 15 kV at a working distance of 10.0 mm. Spot energy dispersive spectroscopy measurements were collected with a Thermo-Noran Vantage microanalysis system. The diameter of the interaction volume for elemental measurements is *ca.* 2.0 µm for oxide and sulfide minerals. Matrix correction coefficients (*Z*, *A* and *F*) were calculated using the Phi(Rho*z) method of Pouchou & Pichoir (1984) and Bastin & Heijligers (1991). X-ray spectra were collected using counting times of 60 s and a probe current of 20 nA.

The electron backscatter diffraction data show the *c*-axis of the MSM17951 pyrrhotite is oriented almost normal (77°) to the sample's surface. We arbitrarily defined one of the a-axes to be $a_1 = 0°$. With reference to this axis, the *c*-axis trends 286° and the two other *a*-axes lie close to expected pseudo-hexagonal structure directions that trend $a_2 = 57°$ and $a_3 = 116°$ with respect to a_1. We estimate a ±5° uncertainty on the relative alignment defined by the crystallographic axes from the EBSD measurements with respect to the magnetic hysteresis measurements described below. Close examination of the sample surface at high magnification using both secondary and backscattered electrons, as well as a fore-scatter detector, revealed no evidence for twinning, intergrowths or mineral inclusions. Nine spot energy dispersive spectra yield an average composition of 47.4 ± 0.7 at.% Fe and 52.6 ± 0.7 at.% S, corresponding to a bulk chemical composition of $Fe_{7.2\pm0.2}S_8$.

The samples used for the temperature cycling experiments comprise three pyrrhotite-bearing gneiss samples (P167, P512 and P527) from the Kirchzarten deep drilling project in the Black Forest, Germany (Pucher & Fromm 1985) and a pure polycrystalline pyrrhotite sample (MSM73410) from Schmiedeberg, Germany with a chemical composition of $Fe_{7.0}S_8$ courtesy of the Mineralogical State Collection. Mössbauer spectra, magnetic hysteresis, Curie and Besnus temperature measurements for MSM73410 were reported in Gilder *et al.* (2011). Thermomagnetic curves measured with a Petersen Instruments variable field translation balance define Curie temperatures of 319 ± 5 °C for the three samples from the gneisses and 322 °C for MSM73410, typical of pure monoclinic pyrrhotite (Dunlop & Özdemir 1997). No lambda transition or Curie temperatures corresponding to magnetic phases other than pyrrhotite were detected.

2.2 Rock magnetic measurements

Magnetic hysteresis loops and backfield curves were measured to maximum fields of 1.5 T with a Princeton Measurements Corporation vibrating sample magnetometer (VSM, University of Minnesota) to obtain remanent saturation magnetization (M_{rs}), saturation magnetization (M_{s}), bulk coercive force (B_{c}) and the coercivity of remanence (B_{cr}) (Fig. 1 and Table 1). Fig. 1(c) plots

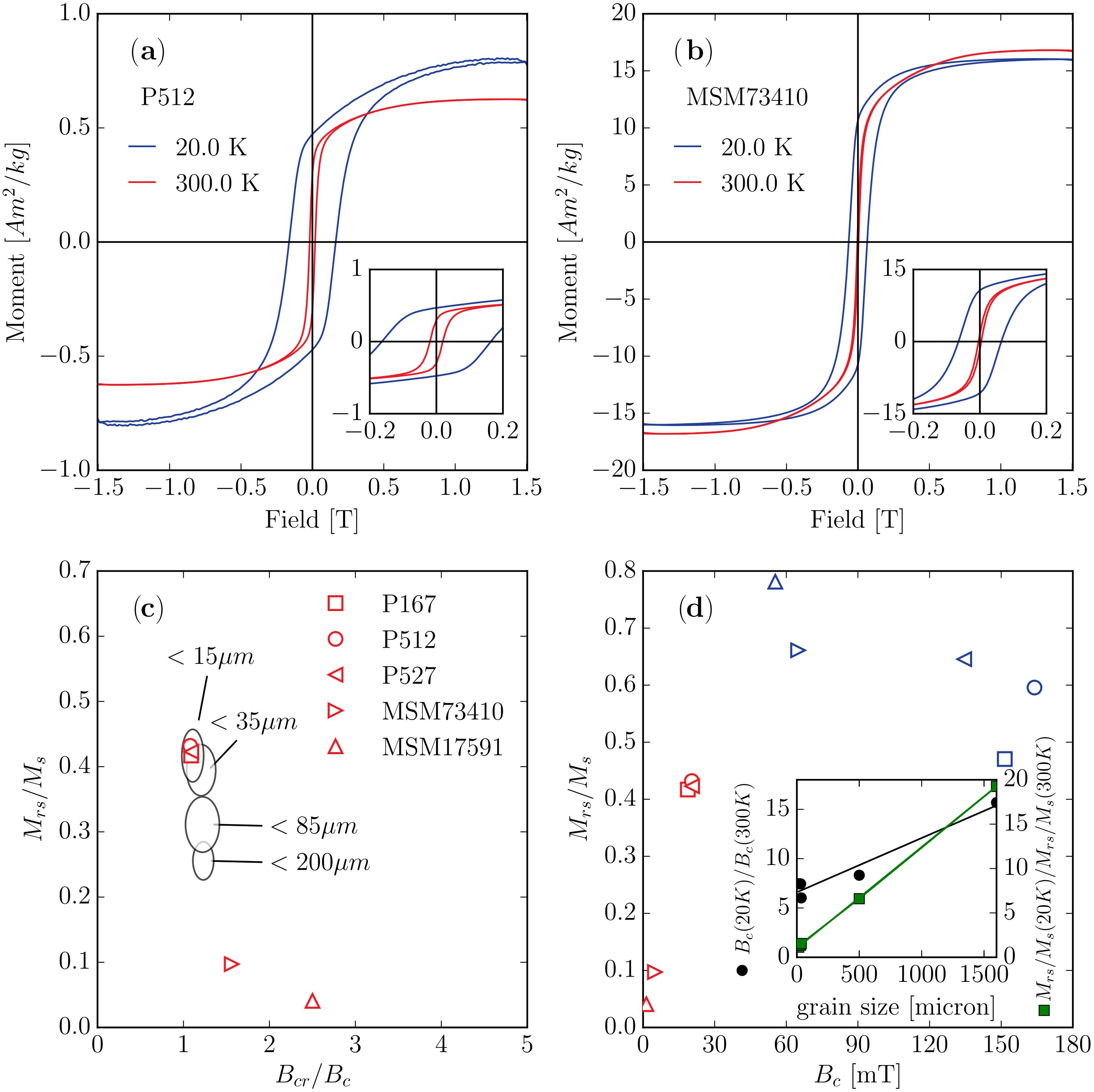

Figure 1. Hysteresis loops measured at 300 and 20 K for samples that are (a) pseudo-single-domain (P512) and (b) multidomain (MSM73410) dominated pyrrhotite after correction for paramagnetic contribution. (c) Day *et al.* (1977) plot for pyrrhotite measured at 300 K. Ellipses represent fields measured from constrained size populations (two standard deviations) of pyrrhotite powder from Dekkers (1988). (d) Comparison of the remanence ratio ($M_{\mathrm{rs}}/M_{\mathrm{s}}$) versus bulk coercivity (B_{c}) measured at 300 K (red points) and 20 K (blue points). Inset shows the relative change (20 K/300 K) in B_{c} and $M_{\mathrm{rs}}/M_{\mathrm{s}}$ as a function of grain size.

the room temperature (300 K) remanence ($M_{\mathrm{rs}}/M_{\mathrm{s}}$) and coercivity ($B_{\mathrm{cr}}/B_{\mathrm{c}}$) ratios together with specific size fractions of pyrrhotite studied by Dekkers (1988). The three samples from the deep bore hole have relatively high remanence ratios ≈0.4 and low coercivity ratios (<1.5) typical of PSD pyrrhotite with grain sizes <35 µm. MSM73410 and MSM17591 have lower $M_{\mathrm{rs}}/M_{\mathrm{s}}$ and higher $B_{\mathrm{cr}}/B_{\mathrm{c}}$ characteristic of MD pyrrhotite with grain sizes >200 µm (Dekkers 1988). Grain sizes listed in Table 1 for the MD-dominated pyrrhotite were estimated by extrapolating the Dekkers (1988) data.

Hysteresis parameters are markedly different above and below T_{Bes} (Table 1 and Fig. 1), consistent with previous work (Dekkers *et al.* 1989; Kind *et al.* 2013). At low temperatures, the MD crystals act more SD like with higher coercivities and remanence ratios. From our limited data, there seems to be a linear relationship between the remanence ratio and B_{c} with respect to grain size (Fig. 1d inset).

For the low-temperature demagnetization experiments, each sample was initially magnetized in a 1 T magnetic field to produce a room temperature ($T_0 = 300$ K) isothermal remanent magnetization

Table 1. Room temperature and 20 K results of hysteresis and backfield measurements. T_{Bes} was calculated from the maximum inflection of $dM(T)/dT$ except for MSM17591 where it was calculated from the maximum inflection in $dBc(T)/dT$ marked by *. Grain sizes for the multidomain-rich pyrrhotite were estimated by extrapolating the Dekkers (1988) data.

Sample	T_c	T_{Bes}	M_s (Am^2 kg^{-1})		M_{rs} (Am^2 kg^{-1})		M_{rs}/M_s		B_c (mT)		B_{cr} (mT)	B_{cr}/B_c
(≈size)	(°C)	(K)	300 K	20 K	300 K	20 K	300 K	20 K	300 K	20 K	300 K	300 K
P167 (15 μm)	325	29	0.35	0.44	0.15	0.208	0.42	0.48	18.7	151.9	20.4	1.09
P512 (30 μm)	314	31	0.64	0.79	0.28	0.472	0.43	0.59	20.4	164.0	22.0	1.08
P527 (35 μm)	317	30	0.27	0.29	0.12	0.187	0.42	0.65	20.6	134.8	22.4	1.09
MSM73410 (0.5 mm)	322	29	16.79	16.01	1.74	10.6	0.10	0.66	5.0	64.9	7.8	1.56
MSM17591 (1.6 mm)	311	30*	21.04	20.48	0.81	15.7	0.04	0.77	1.4	54.9	3.5	2.50

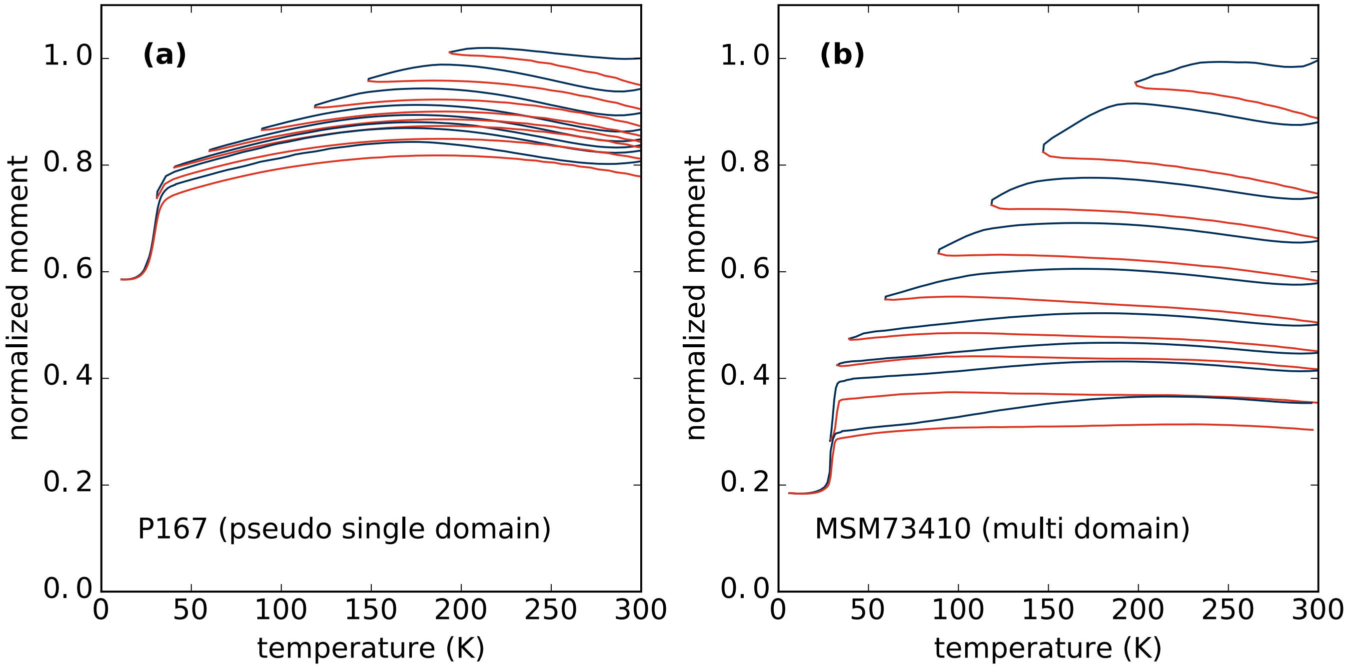

Figure 2. Continuous cooling/warming measurements for (a) pseudo-single-domain-dominated pyrrhotite and (b) multidomain-dominated pyrrhotite. Blue lines are cooling paths from $T_0(=300\ \mathrm{K}) \rightarrow T_i$; red lines show warming back to 300 K.

(IRM). The specimens were cycled from T_0 to one of eight temperatures ($T_i \approx 200$, 150, 120, 90, 60, 40, 30 and 20 K) and then warmed back to T_0 with a VSM. Magnetic moments were measured in 5 K intervals in a zero field. For each cycle, magnetization decreases a few per cent upon initial cooling from 300 K and then slightly increases before decreasing again upon further cooling (Fig. 2). A positive inflection coincides with changes in crystalline anisotropy constants that achieve maximum values around 200 K (Bin & Pauthenet 1963).

The main difference between PSD and MD-dominated samples upon low-temperature cycling is their relative loss in magnetization, which is significantly less in PSD than in MD samples (Fig. 2). In contrast to magnetite, the cooling path does not trace the warming path of the previous cycle. The greatest loss in remanence occurs at the Besnus transition. Defined by the maximum in dM/dT calculated from the cooling path of the final $T_0 \rightarrow T(20\ \mathrm{K})$ cycle, T_{Bes} averages 29.8 ± 0.6 K (Table 1), consistent with reported values (30–34 K) (e.g. Rochette *et al.* 1990).

Fig. 3 plots the remaining fraction of initial magnetization after cycling from $T_0 \rightarrow T_i \rightarrow T_0$ as a function of T_i, again showing that demagnetization levels are grain size dependent. Linear regression of the magnetization loss for $T_i > T_{\mathrm{Bes}}$ for the PSD samples averages −7 per cent/100 K, whereas that for the MD sample is roughly four times steeper (−27.8 per cent /100 K). These results agree well with low-temperature demagnetization experiments on MD monoclinic pyrrhotite measured using a low-temperature insert in a cryogenic rock magnetometer (Feinberg *et al.* 2015). Low-temperature demagnetization with liquid nitrogen (see dashed line in Fig. 3), as it is often used in palaeomagnetism would remove ≈45 per cent of the remanence carried by MD grains. Remanence carried by PSD particles on the other hand will only be lowered by 8–16 per cent when cooled to 77 K. For temperature cycling to 150 K from 300 K, PSD and MD magnetite lose much more magnetization [45 and 55 per cent, respectively; Dunlop (2003)] in comparison to pyrrhotite (10 and 25 per cent). Moreover, thermal remanent magnetization in PSD magnetite is harder (demagnetizes less than) to low-temperature demagnetization than a 1 T IRM (Dunlop 2003). If the same is true for pyrrhotite, then palaeointensity estimates from meteorites whose magnetizations are carried by single to PSD pyrrhotite should

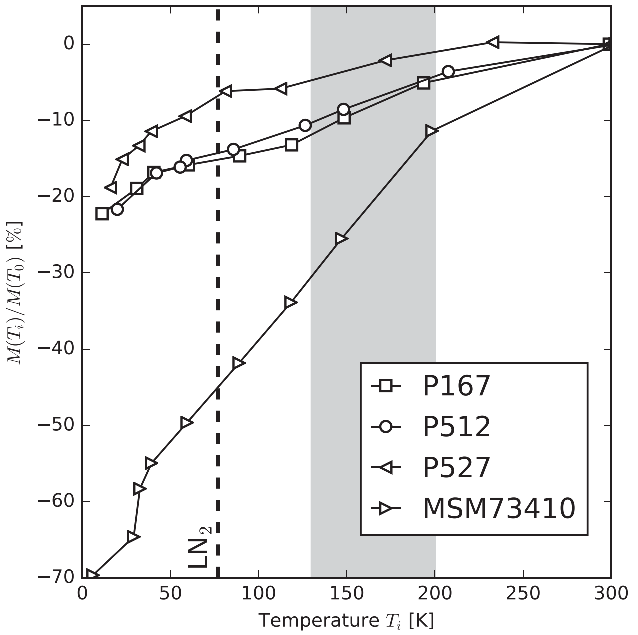

Figure 3. Stepwise demagnetization of a 1 T isothermal remanent magnetization (IRM). A room temperature IRM was cycled from $T_0 \rightarrow T_i \rightarrow T_0$. The recovered magnetization at room temperature is plotted as a function of T_i. Shaded area shows likely equilibrium temperatures of a rotating meteorite at 3.5 AU distance from the sun. Dashed line shows liquid nitrogen (LN$_2$) temperature (77 K).

be lowered by less than 10 per cent when temperature cycled to 150 K.

A pronounced inflection is visible in the demagnetization curves at the Besnus transition (Fig. 2). Dekkers *et al.* (1989) cooled pyrrhotite with different crystal sizes to 4.2 K through the Besnus transition and then warmed them back to room temperature in a null field. They found that the recovered remanence at 300 K after a full 4.2 K cycle depended on grain size, with smaller particles retaining more magnetization than larger ones. Comparing the remanence recovered after cycling to 20 K, the PSD-dominated rock samples in our study show a recovery similar to that of grains <35 µm in Dekkers *et al.* (1989). The large crystal (MSM73410), however, recovers less than the largest sample studied by Dekkers *et al.* (1989). For a MD sample that had been cycled through the transition, and then cycled a second time, the recovery could be erroneously interpreted as a sign of a sample rich in single or PSD particles.

2.3 Hysteresis parameters as a function of direction and temperature

To better understand the mechanism controlling the Besnus transition, we measured hysteresis loops and backfield curves at one or two K intervals from 50 to 20 K as well as at 300 K along 72 directions in the basal plane of the single crystal (disc). Hysteresis loops were corrected for field and moment offsets following von Dobeneck (1996). In order to remove potential bias from misalignment or field offsets inside the magnetometer, we assumed that the measurements along antipodal directions (±180°) were equal and averaged their moments. The sample was never removed from the magnetometer during the entire course of the experiments in order to avoid potential sample misalignment.

When measured along one of the crystallographic *a*-axes at 300 K, the moment sharply increases up to 25 mT and then gradually approaches saturation in a fairly curved manner (blue curve in Fig. 4a). Rotating the sample 30° in-between two *a*-axes (green curve in Fig. 4a) results in a lower initial rise in moment below 25 mT followed by a steeper approach to saturation. That M_s is not identical in all directions at some temperatures suggests 1.5 T does not always fully saturate the sample; hence, the moment at 1.5 T will be referred to as pseudo-M_s (M_s*). The lowest and highest values for M_s* (20.8 and 21.2 Am^2 kg^{-1}) at 300 K lie within the range of reported values (18.3–21.2 Am^2 kg^{-1}) (O'Reilly *et al.* 2000; Kind *et al.* 2013). Except for the steep initial rise in moment below 25 mT that persists at all temperatures, the character of the hysteresis loops change considerably within the basal plane above (Fig. 4b), during (Fig. 4c) and below (Fig. 4d) T_{Bes}. Each case is discussed separately below.

2.4 Magnetic behaviour above T_{Bes} (>34 K)

The curvature in the hysteresis loops along the *a*-axes diminishes considerably approaching T_{Bes} (blue curve in Fig. 4b), whereas an intriguing double inflection arises between *a*-axes (green curve in Fig. 4b). Loops with double inflections appear with sixfold symmetry between *a*-axes, although one direction (160°–340°) is more pronounced than the other two. The closer the measurement direction is to an *a*-axis, the higher the field at which the inflection appears (B_{inf}) and the less pronounced it becomes. Defining B_{inf} by the peak in dM/dB of the downfield branch (crosses in Fig. 5) shows that B_{inf} appears at around 185 K and remains constant at a field of 470 mT down to 120 K. At approximately 200 K, the anisotropy constant K4 reaches a maximum and K3 changes sign (Bin & Pauthenet 1963), only a few kelvin away from the appearance of the second inflection. At temperatures lower than 100 K B_{inf} reaches a maximum of 780 mT at 40 K. Below 40 K, the peak rapidly disappears with a progressive decrease in B_{inf} from 700 mT at 36 K to 300 mT at 33 K before disappearing at 32 K. M_s* is higher where the double inflection is most pronounced (Fig. 4b). Koulialias *et al.* (2016) also found a double inflection in a single crystal of Fe$_7$S$_8$; however, they measured their sample only in one direction, most likely between *a*-axes, which made it impossible to see the directional dependence of the inflection. Koulialias *et al.* (2016) noted a shift in B_{inf} from 500 mT at 200 K to 750 mT at 40 K, the latter being consistent with our results.

Normalizing the hysteresis parameters to their maximum and minimum values, so that the values range from 1 to 0, more clearly shows their expression as a function of measurement angle (Fig. 6). At 50 K ≥ $T > T_{\mathrm{Bes}}$ all maxima in hysteresis parameters fall between crystallographic axes. M_s* peaks at 155°, 25° away from a crystallographic *a*-axis, similar to the findings of Wolfers *et al.* (2011); the minimum in M_s* lies at 120°, nearest to the *a*-axis that projects in the *c*-axis direction (106°). All local minima in M_s* trend close to crystallographic *a*-axes, with sixfold symmetry. Between 300 and 34 K, the sixfold symmetry persists and the average M_s* stays constant although the maxima and minima are more pronounced at 50 K then below according to the standard deviation of 36 M_s* values (Table 2). The maximum in bulk coercivity (B_c) (2.0 mT) occurs near the M_s* maximum while the minimum in B_c (1.2 mT) is orthogonal with a uniaxial expression. B_c and B_{cr} maxima nearly coincide at 300 K. At 50 K and below, B_c and B_{cr} maxima diverge, with B_c trending nearly parallel to M_s* while B_{cr} maximizes at the *a*-axis that coincides nearest to the *c*-axis with a second maxima in another *a*-axis direction. Saturation remanence (M_{rs}) defines two maxima at 300 K: a submaximum (1.18 Am^2 kg^{-1}) parallel to the

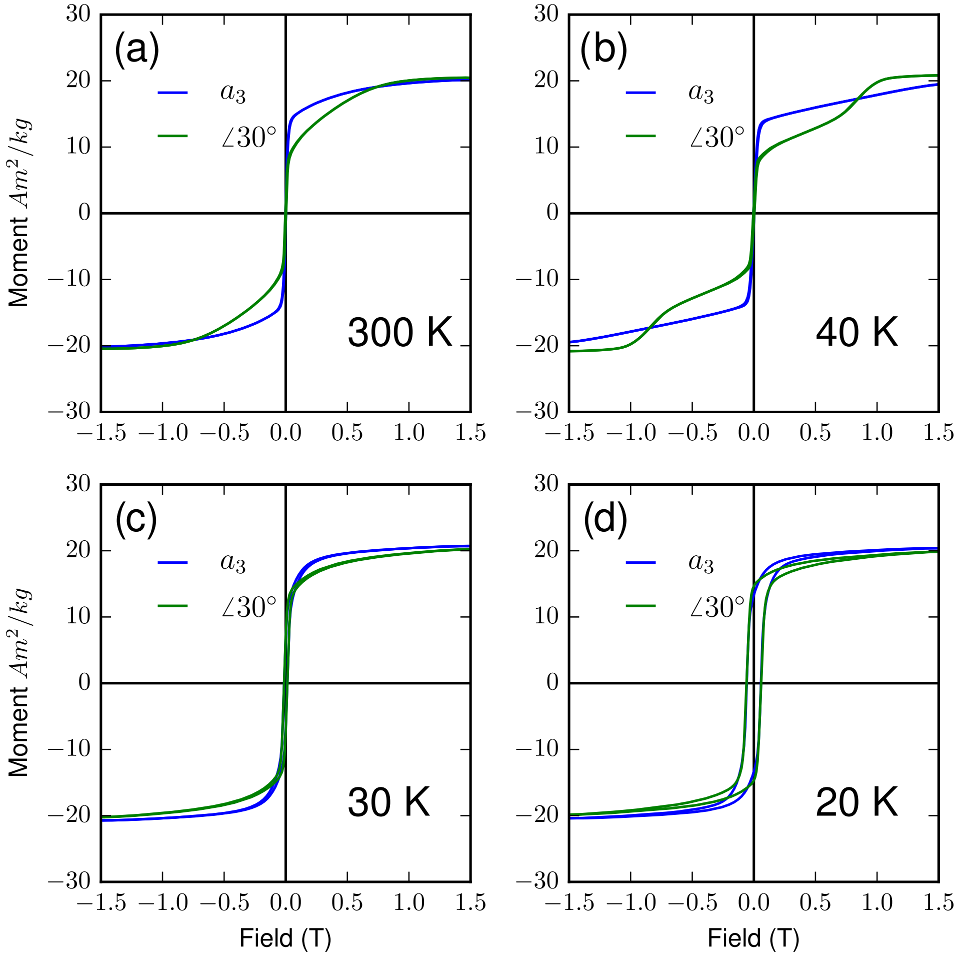

Figure 4. Hysteresis loops of MSM17591 at (a) 300 K, (b) 40 K, (c) 30 K and (d) 20 K measured along the crystallographic *a*-axis (blue) and at an angle 30° away from the *a*-axis (green).

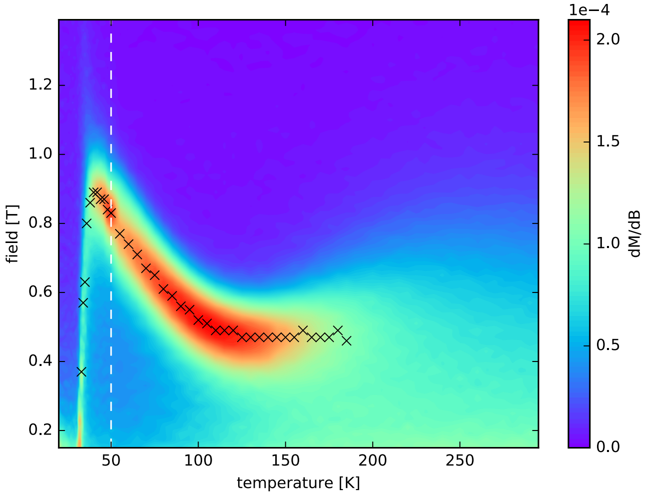

Figure 5. First derivative (*dM*/*dB*) plot of the 165° downfield branch of the hysteresis measurements. Red patches show the appearance of the second inflection. Crosses mark the maximum of the first derivative. Data at temperatures above 50 K (dashed white line) were acquired at LMU-Munich, below 50 K at IRM-Minnesota.

c-axis and the maximum (1.28 Am^2 kg^{-1}) orthogonal to it. By 50 K and below, the submaximum in M_{rs} disappears and lies squarely between two a-axes.

2.5 Magnetic behaviour within T_{Bes} (34–28 K)

Hysteresis loops and hysteresis parameters, except for M_{s}* and B_{rh} [the median destructive field of remanent hysteresis; von Dobeneck (1996)], change markedly between 34 and 28 K (Table 2, and Figs 4c and 7). M_{s}* slightly, yet almost imperceptibly, increases through the transition with a minimum in standard deviation at 34 K; the standard deviation for B_{rh} is lowest at 31 K. B_{c} and M_{rs} increase prominently across T_{Bes} on cooling, which best define the transition temperature region with both dB_{c}/dT and dM_{rs}/dT showing maxima at 30 K for all angles. We conclude that these two parameters best define the transition temperature, while the transition itself spans about 6 K. Within the transition, maxima in B_{cr} and B_{c} parallel each other between two *a*-axes; M_{s} rotates *ca.* 60°, closer into coincidence with M_{rs} (Fig. 6).

Surprisingly, B_{c} increases faster than B_{cr}, and by 30 K, B_{cr} actually becomes lower than B_{c} thereby reducing the coercivity ratio below unity. To our knowledge, this is the first time a coercivity ratio below unity has been reported, which leads one to question whether it is due to an experimental artefact. However, this observation is highly reproducible, being based on 360 backfield measurements

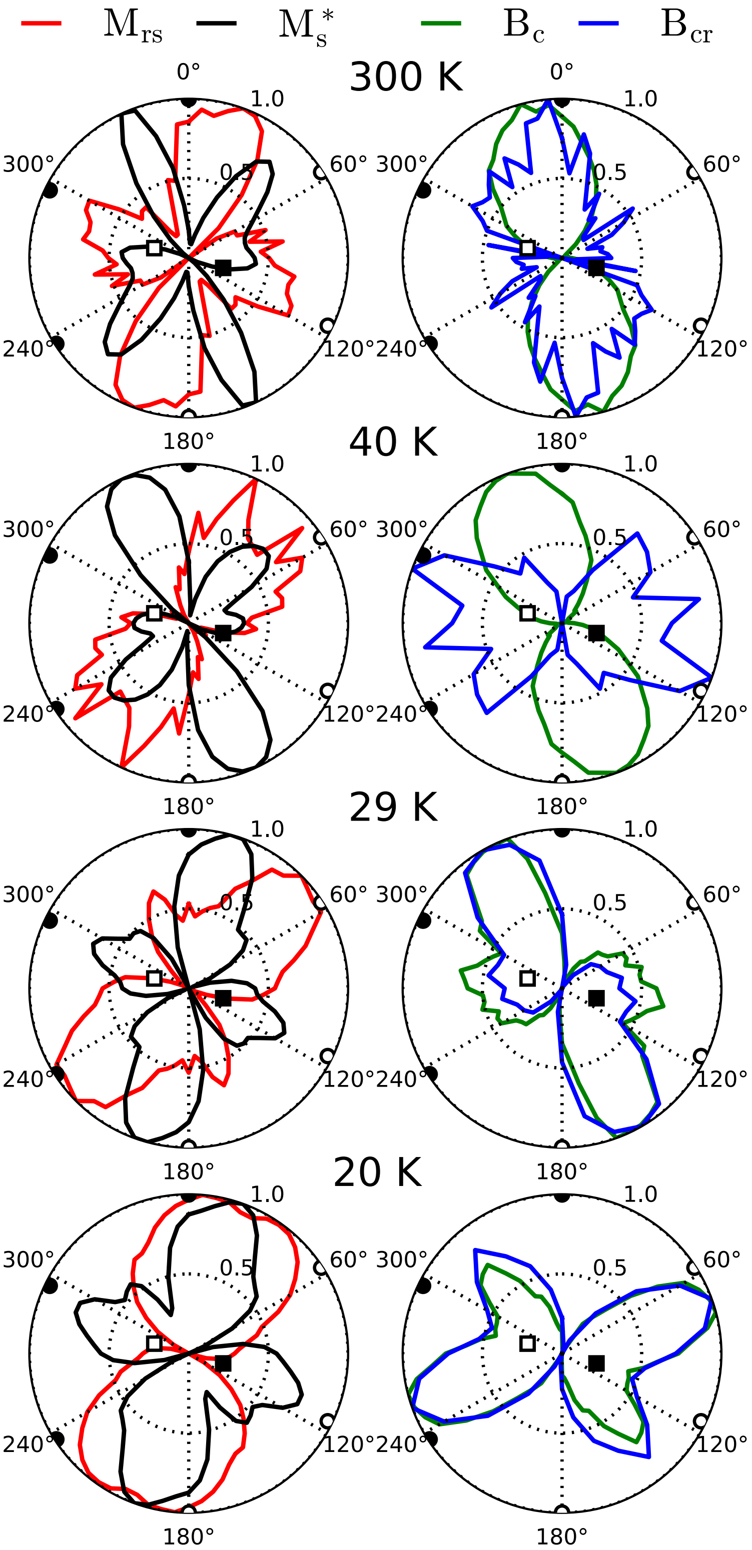

Figure 6. Magnetic hysteresis and backfield parameters of the single crystal MSM17591 normalized by their minimum and maximum values at four discrete temperatures. Circles indicate the crystallographic *a*-axes and the squares represent the *c*-axis measured at 300 K; filled symbols lower hemisphere, open symbols upper hemisphere.

Table 2. Average results calculated from all measurement directions for the single crystal disc MSM17591. $N = 72$ for M_s, M_{rs}, B_c and $n = 36$ for B_{cr}. Backfield curves were not measured for temperatures >40 K. Uncertainties are one standard deviation.

T (K)	M_{rs} (Am^2 kg^{-1})	M_s* (Am^2 kg^{-1})	M_{rs}/M_s	B_{cr} (mT)	B_c (mT)	B_{cr}/B_c
300	1.16 ± 0.04	20.96 ± 0.11	0.06 ± 0.002	2.92 ± 0.34	1.52 ± 0.29	1.96 ± 0.24
50	1.79 ± 0.08	20.73 ± 0.53	0.09 ± 0.004		3.24 ± 0.48	
48	1.73 ± 0.07	20.66 ± 0.53	0.08 ± 0.004		3.18 ± 0.47	
46	1.58 ± 0.05	20.72 ± 0.52	0.08 ± 0.003		3.13 ± 0.49	
44	1.58 ± 0.04	20.74 ± 0.51	0.08 ± 0.003		3.18 ± 0.51	
42	1.58 ± 0.04	20.70 ± 0.48	0.08 ± 0.003		3.23 ± 0.51	
40	1.58 ± 0.04	20.72 ± 0.43	0.08 ± 0.003	7.79 ± 0.32	3.28 ± 0.52	2.44 ± 0.45
38	1.59 ± 0.05	20.79 ± 0.36	0.08 ± 0.003	7.94 ± 0.42	3.33 ± 0.53	2.44 ± 0.43
36	1.60 ± 0.04	20.87 ± 0.26	0.08 ± 0.002	8.12 ± 0.38	3.39 ± 0.54	2.45 ± 0.42
35	1.62 ± 0.05	20.97 ± 0.19	0.08 ± 0.002	8.10 ± 0.38	3.46 ± 0.55	2.40 ± 0.40
34	1.64 ± 0.05	20.97 ± 0.16	0.08 ± 0.002	8.27 ± 0.37	3.53 ± 0.56	2.39 ± 0.38
33	1.77 ± 0.05	21.11 ± 0.20	0.08 ± 0.003	8.58 ± 0.36	3.80 ± 0.59	2.30 ± 0.33
32	2.24 ± 0.08	21.20 ± 0.24	0.11 ± 0.004	9.13 ± 0.46	4.72 ± 0.66	1.96 ± 0.19
31	4.00 ± 0.18	21.30 ± 0.25	0.19 ± 0.009	9.96 ± 0.94	7.15 ± 0.63	1.39 ± 0.05
30	7.61 ± 0.38	21.24 ± 0.28	0.36 ± 0.019	12.04 ± 1.13	12.38 ± 0.64	0.97 ± 0.05
29	10.39 ± 0.54	21.22 ± 0.32	0.49 ± 0.028	15.54 ± 1.01	16.94 ± 0.80	0.92 ± 0.02
28	11.77 ± 0.57	21.09 ± 0.36	0.56 ± 0.031	17.71 ± 1.02	19.95 ± 1.12	0.89 ± 0.02
27	12.24 ± 0.54	21.08 ± 0.38	0.58 ± 0.031	19.10 ± 1.09	21.58 ± 1.26	0.89 ± 0.02
26	12.87 ± 0.64	21.01 ± 0.41	0.61 ± 0.034	21.28 ± 1.27	24.56 ± 1.42	0.87 ± 0.02
24	13.86 ± 0.73	20.95 ± 0.44	0.66 ± 0.037	27.44 ± 1.75	33.09 ± 1.95	0.83 ± 0.01
22	14.51 ± 0.77	20.91 ± 0.46	0.69 ± 0.037	35.04 ± 1.94	43.96 ± 2.39	0.80 ± 0.01
20	15.00 ± 0.77	20.87 ± 0.47	0.72 ± 0.036	46.75 ± 2.48	57.11 ± 2.72	0.82 ± 0.01

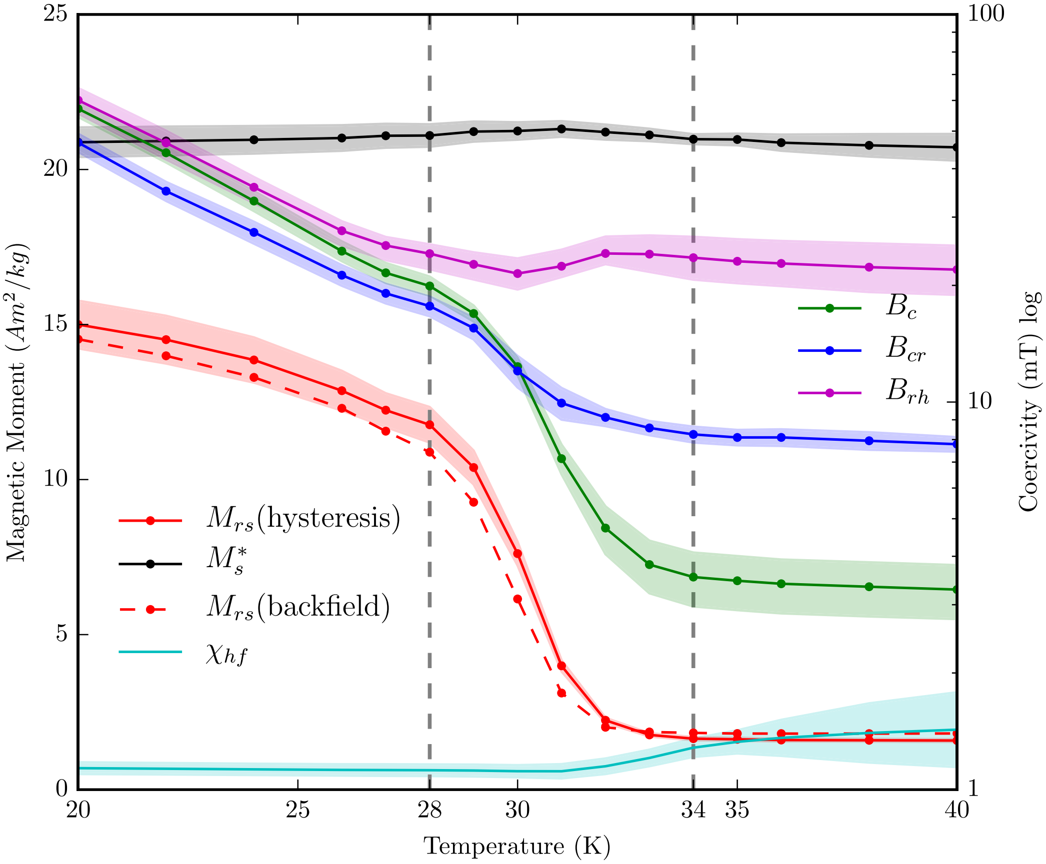

Figure 7. Average hysteresis parameters for 72 hysteresis and 36 backfield measurements at each temperature step between 40 and 20 K. Shaded regions show one standard deviation. Vertical lines represent the Besnus transition temperature range as defined in the text. Dashed red line shows SIRM (=M_{rs}) values calculated from the backfield measurements, uncertainty envelope omitted for clarity. Coercivity (B_c, B_{cr}, B_{rh}) is plotted on a log scale.

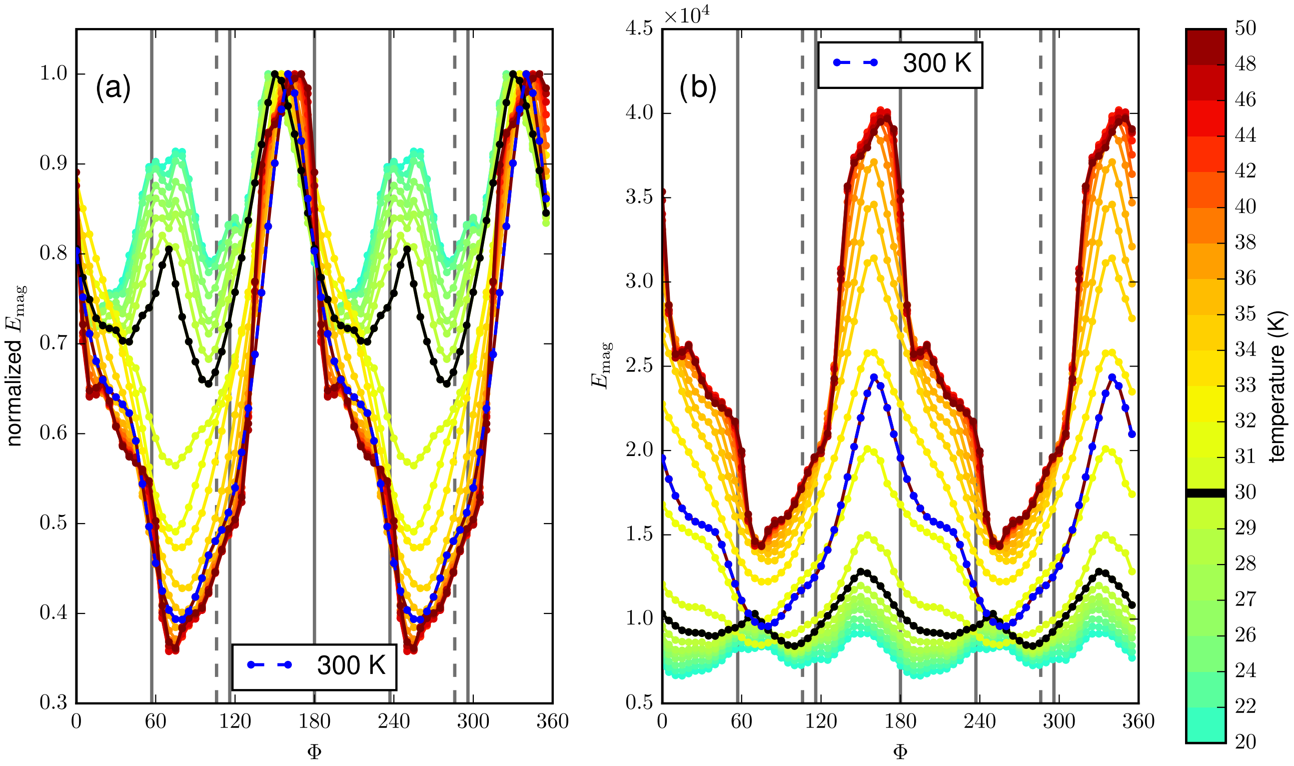

Figure 8. (a) Normalized magnetizing energy and (b) magnetizing energy calculated by integrating over all moments of the descending branch at positive fields. Lines show the crystallographic a-axes with respect to the a_1-axis at 0°. The dashed line shows the projection of the crystallographic c-axis on the basal plane. Room temperature values in blue.

with corresponding hysteresis loops. Although an offset in field or magnetic moment could lower $B_{\rm cr}$ values, the bias would have to be very large (up to 20 per cent $B_{\rm cr}$) to underestimate a field of $\approx$11 mT at 20 K.

Another possible explanation is a faulty temperature measurement. To test this, we measured hysteresis loops and backfield curves in different sequences but still found lower $B_{\rm cr}$ values. Moreover, the phenomenon has been replicated in two separate laboratories, where measurements between 20 and 29 K in two different angles on a VSM at the University of Munich yielded the same conclusion: coercivity ratios below unity.

Backfield curves of a non-saturated sample could lead to an underestimate of $B_{\rm cr}$. Although the value for $M_{\rm rs}$ obtained from backfield measurements (dashed red line in Fig. 7) is slightly lower than $M_{\rm rs}$calculated from hysteresis loops below 33 K, correcting the backfield curve for this difference cannot account for the coercivity ratio lying below unity. In many cases, the backfield curve would have to be corrected by such a large amount (*ca.* 40 per cent at 20 K), that $M_{\rm rs}$ determined from backfield measurements would well exceed $M_{\rm rs}$ derived from hysteresis loops (*ca.* 25 per cent at 20 K). Furthermore, the high-field susceptibility ($\chi_{\rm hf}$), calculated from a linear regression of the moments at $|B| \geq 1.3$ T decreases at 33 K which indicates that the sample is closer to saturation than at temperatures above the transition (Fig. 7). In summary, we find no experimental ground to explain away the observation that $B_{\rm cr}/B_{\rm c}$ is less than one below $T_{\rm Bes}$.

2.6 Magnetic behaviour below $T_{\rm Bes}$ (<28 K)

Hysteresis loops widen appreciably below $T_{\rm Bes}$ as $B_{\rm c}$ increases markedly (Fig. 4d), and the symmetry changes from six to fourfold (see below). Measurement directions in between two a-axes lose the double inflection and show a more gradual approach to saturation. Maxima in $B_{\rm c}$ and $B_{\rm cr}$ remain parallel, yet lie nearly orthogonal to their pre-$T_{\rm Bes}$ directions and exhibit distinct submaxima (Fig. 6). Both develop a second peak at $\approx$80°. The maxima of $M_{\rm s}$* align perpendicular to the c-axis projection. Saturation remanence continues to increase below 28 K, but at a lower rate than during the transition (Fig. 7), while coercivity increases linearly when plotted on a log scale.

2.7 Symmetry considerations

The magnetic easy and hard axes correspond to the direction with the lowest and highest magnetization energies (Dunlop & Özdemir 1997). To calculate the crystalline anisotropy, the maximum applied field during the course of a hysteresis loop should exceed the anisotropy field, otherwise the crystal will not become fully saturated. Although 1.5 T does not quite saturate the crystal, we calculated the magnetizing energy ($E_{\rm Mag} = \int_0^{M_s^*} B\, dM$) from the positive downfield branch for all angles and temperatures. Fig. 8(a) plots the normalized magnetizing energy as a function of angle in the basal plane; Fig. 8(b) shows the unnormalized values. While these energies cannot be used to calculate the anisotropy constants, they can indicate the position of the easy axis within the basal plane when the energy attains a minimum. The maximum energy does not indicate the hard axis as it lies perpendicular to the basal plane—at least above $T_{\rm Bes}$ (Bin & Pauthenet 1963). Only one dominant easy axis exists above the transition, trending about 20° away from the a_2-axis. $M_{\rm s}$* is directionally independent in a fully saturated sample; however, it is interesting that the maximum energy coincides with

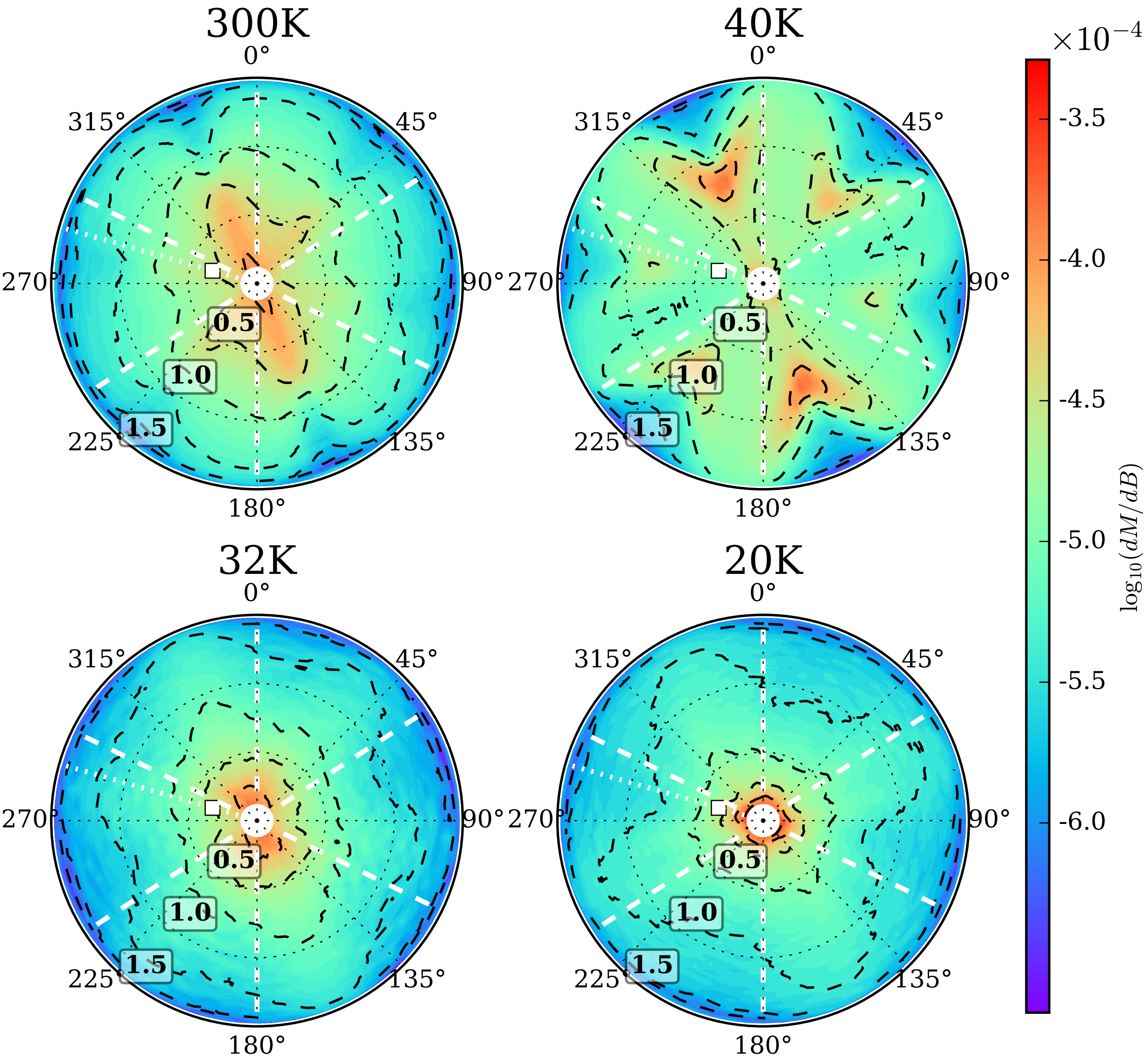

Figure 9. Angular dependence of the first derivative of the ascending branches of the hysteresis loops at four temperatures. Radial distance corresponds to the field value in T, as indicated by the labelled black dashed lines. The central area ($B < 30$ mT) was omitted for clarity. White dashed lines indicate the crystallographic *a*-axes. Dotted white line and square represent the *c*-axis and its projection on the basal plane. A hexagonal pattern is apparent in the data between 50 and 34 K with the second inflections aligned between *a*-axes.

the maximum of M_s* and B_c at 160°. The easy axis stays constant to within ±5° until 30 K and then abruptly rotates 25°. Both the mean energy as well as the difference between minimum and maximum energy states decrease. The location of the minimum energy at 300 K converts at 30 K into a local maximum with two local minima occurring below T_{Bes}, likely indicative of two, orthogonal easy axes.

The rotational symmetry of the second inflection in the hysteresis loops (Fig. 4b) can be best visualized using the first derivative of the ascending branches (Fig. 9). As above, the second inflection is not visible at room temperature in accordance with Koulialias *et al.* (2016). A gap between 300 and 50 K in our study precludes the onset temperature for the second inflection; however, at 50 K, local maxima in the *dM*/*dB* curves clearly show a sixfold symmetry dictated by the *a*-axes. Not only are the directions consistent with M_s* maxima, but also their magnitudes, with the strongest inflection coincident with the greatest M_s*. The peaks in the derivative show a V-shaped pattern aligned with the crystal structure. A likely explanation for the origin of the second inflection is a field induced flipping of the easy axis as suggested by Bin & Pauthenet (1963), who measured the crystalline anisotropy of a spherical Fe_7S_8 crystal. Their calculations of the crystalline anisotropy broke down below 60 K, which they attributed to field induced change in the easy axis direction. The hexagonal pattern disappears around 33 K and then a fourfold symmetry appears below 29 K.

Using the descending branch at positive fields of the hysteresis measured along the dominant axis ($\phi_0 = 75°$) at room temperature as a reference ($M(T_0, B^+, \phi_0)$), we calculated the relative differences to it for all branches measured along other directions (ϕ_n) with:

$$\Delta M(T, B^+, \phi_n) = \left[M(T, B^+, \phi_n)/M(T_0, B^+, \phi_0)\right] - 1$$

in per cent (Fig. 10). Blue colours show regions where the magnetization of the hysteresis branch when measured along ϕ_n is smaller than ϕ_0 for a given field, while red colours show higher moments

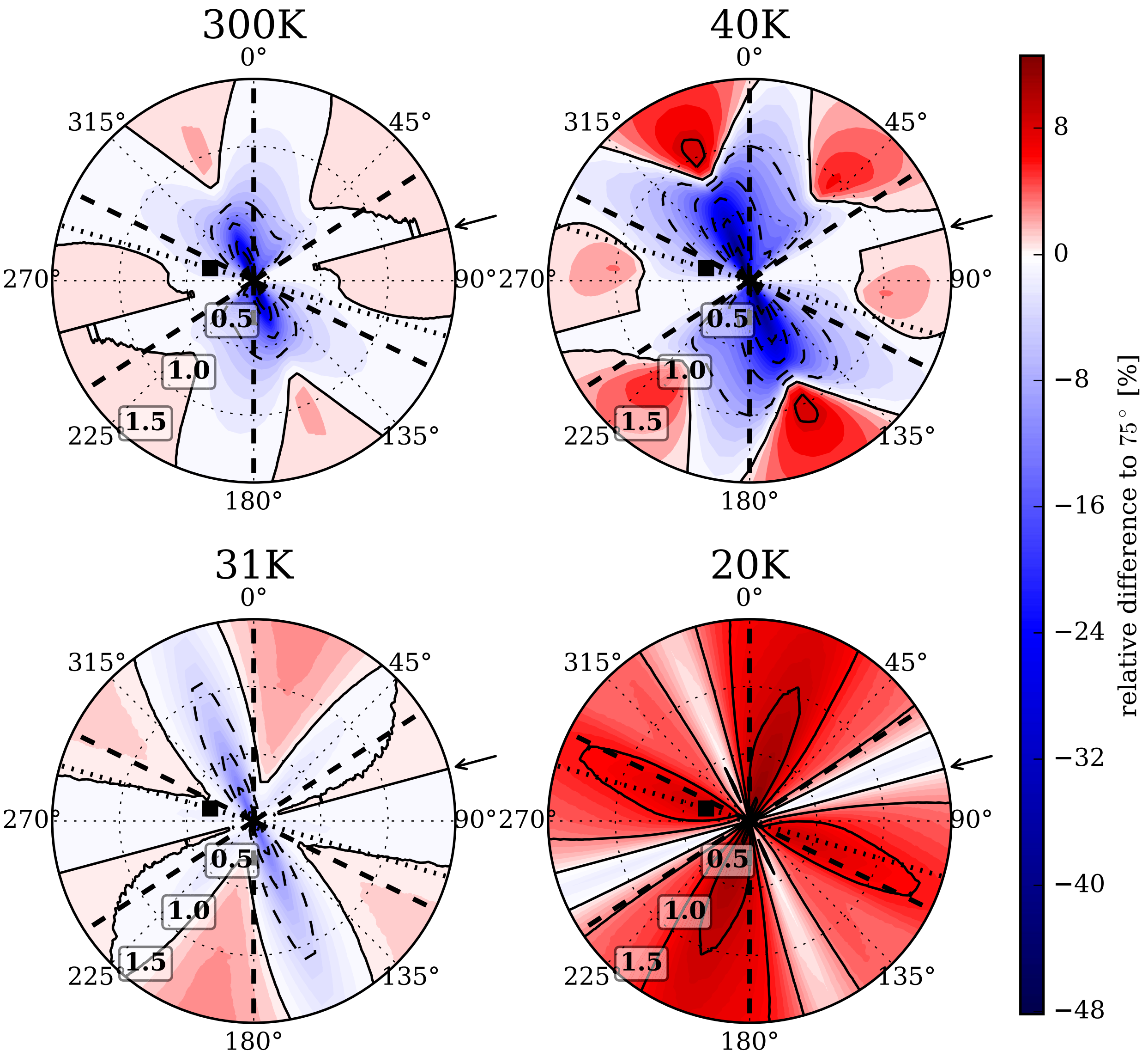

Figure 10. Relative difference of the positive downfield branch of each measurement direction with respect to the easy direction at room temperature ($\phi_0 = 75^\circ$) for selected temperatures. Arrow points along ϕ_0. Red colours show a positive, blue colours show negative lower magnetic moments. Radial distances correspond to the magnetic field in T.

($M(T, B^+, \phi_n) > M(T_0, B^+, \phi_0)$). In other words, blue colours indicate harder than average magnetization energies and red, lower. Similar to the derivatives, the relative differences show a hexagonal pattern at temperatures above the Besnus transition. They also show that the moments measured along the magnetic hard axis (160°) are larger than when measured along the easy axis at fields >0.6 T. This behaviour is even more apparent at temperatures from 50 K to T_{Bes} and coincides with the second inflections as seen in the derivatives. At $T < 34$ K, the hexagonal pattern starts to disappear, and by 20 K, the sixfold symmetry has completely disappeared and is replaced by four maxima.

3 DISCUSSION AND CONCLUSIONS

The grain size dependence of the amount of magnetization lost during repetitive cycling of monoclinic pyrrhotite from 300 K to subsequently lower temperatures until below the Besnus transition confirms the work of Dekkers *et al.* (1989). PSD-dominated pyrrhotite loses only ≈10 per cent of a room temperature IRM at 150 K, while MD-dominated pyrrhotite loses ≈28 per cent at 150 K (Fig. 3). The relative amount of magnetization lost is much less than like grain sizes of magnetite (Dunlop 2003). Dunlop (2003) and Halgedahl (1998) showed that thermoremanent magnetizations generally demagnetize less than IRM upon low-temperature cycling. If also true for single to PSD pyrrhotite, then meteorites that thermally equilibrated in space after acquiring a thermal remanence likely retain most of their original magnetization; palaeointensity measurements on them would only slightly underestimate their true intensity. With more temperature cycling experiments, it may be possible to develop a space thermometer to estimate the coldest temperature a meteorite experienced.

From at least 50 K to the Besnus transition, two end-members types of hysteresis loops exist: (1) those resembling magnetic easy axes that quickly saturate by 25 mT and lie parallel to crystallographic *a*-axes and (2) those that show a double inflection with a maximum change in inflection occurring around 750 mT in-between crystallographic *a*-axes. These latter curves more closely resemble magnetic hard axes. Although the pattern of hard and easy axis directions mimics sixfold symmetry, magnetic energy calculations show one of the axes is relatively easier (lower energy) and one harder (higher energy) than the others (Fig. 8). The absolute energy (Fig. 8b) of this easiest axis is more than two times lower and could be due to the slightly monoclinic nature of the crystal but is likely not due to misorientation in the VSM as it is so prominent. The pattern breaks down at T_{Bes}, suggesting independency of the two, similar to the isotropic point in magnetite, where two crystalline anisotropy constants change sign, independent of and $\approx 10^{\circ}$ higher in temperature than the Verwey transition (Hodych 1991). Indeed the analogy is intriguing except that in pyrrhotite the ‘apparent isotropic’ point would be both temperature and field dependent, with the added complication that these dependencies vary with the relative orientation between the crystallographic and applied field directions.

The Besnus transition is characterized by an increase in M_{rs}, B_{c} and B_{cr} on cooling through the 34–28 K range, with the most rapid change in M_{rs} or coercivity occurring at 30 K, similar to previous findings (Fillion & Rochette 1988; Dekkers *et al.* 1989; Rochette *et al.* 1990; Kind *et al.* 2013; Koulialias *et al.* 2016). M_{s}* remains virtually constant through T_{Bes} from 40 to 20 K.

While a magnetophysical description through T_{Bes} seems clear, the mechanism causing T_{Bes} does not. Likely the most important observation lies in Fig. 10 where a clear change from sixfold to fourfold anisotropy occurs. This is further confirmed by the derivative of the loops (Fig. 9). The most likely cause for change in magnetic symmetry is a change in crystallographic symmetry from hexagonal to monoclinic or triclinic, as suggested by neutron diffraction and magnetic torque measurements of Wolfers *et al.* (2011). We observe one axis of easy magnetization in the magnetizing energy above and two easy directions below T_{Bes}, which is compatible with their findings.

An alternative view of the cause of T_{Bes} interprets the second inflection in the hysteresis loops as evidence for a two-phase system (Koulialias *et al.* 2016). Koulialias *et al.* (2016) suggested that epitaxial interactions between the 5C* and 4C magnetic sublattices cause the transition. Our new findings clearly demonstrate a directional dependency of the inflection and its link to the crystallographic *a*-axes, which argue the phenomenon is related to the crystal lattice. These patterns disappear at the Besnus transition and could be interpreted as field induced switching of the easy axis as proposed by Bin & Pauthenet (1963). We therefore conclude that T_{Bes} owes its origin to changes in crystallographic symmetry and anisotropy rather than interacting superstructures.

ACKNOWLEDGEMENTS

This work was supported by Deutsche Forschungsgemeinschaft project WA3402/1-1 and GI712/6-1 under the auspices of SPP1488, Planetary Magnetism. We thank Rupert Hochleitner of the Munich Mineralogical State Collection (Mineralogische Staatssammlung München) and Jean Pohl for providing the samples. Helpful reviews by Ann Hirt and Myriam Kars improved this paper. Editorial handling by Eduard Petrovsky is appreciated. Parts of this work were carried out in the Characterization Facility, University of Minnesota, which receives partial support from NSF through the MRSEC program. We thank Nicholas Seaton for his help in obtaining EBSD and EDS data. Part of this work was performed as a Visiting Fellow at the Institute for Rock Magnetism (IRM) at the University of Minnesota. The IRM is a US National multiuser facility supported through the Instrumentation and Facilities program of the National Science Foundation, Earth Sciences Division, and by funding from the University of Minnesota.

REFERENCES

Bastin, G.F. & Heijligers, H.J.M., 1991. Quantitative electron probe microanalysis of ultra-light elements (Boron-Oxygen), in *Electron Probe Quantitation,* pp. 145–161, eds Heinrich, K.F.J. & Newbury, D.E., Springer.

Bertaut, E.F., 1953. Contribution à l’étude des structures lacunaires: la pyrrhotine, *Acta Crystallogr.,* **6**(6), 557–561.

Besnus, M.J. & Meyer, A.J., 1964. Nouvelles données expérimentales sur le magnétisme de la pyrrhotine naturelle, in *Proc. Int. Conf. Mag.*, Nottingham, Vol. 20, pp. 507–511.

Bezaeva, N.S. *et al.*, 2016. Magnetic characterization of non-ideal single-domain monoclinic pyrrhotite and its demagnetization under hydrostatic pressure up to 2GPa with implications for impact demagnetization, *Phys. Earth planet. Inter.,* **257,** 79–90.

Bin, M. & Pauthenet, R., 1963. Magnetic anisotropy in pyrrhotite, *J. appl. Phys.,* **34**(4), 1161–1162.

Charilaou, M., Kind, J., Koulialias, D., Weidler, P.G., Mensing, C., Löffler, J.F. & Gehring, A.U., 2015. Magneto-electronic coupling in modulated defect-structures of natural Fe1-xS, *J. appl. Phys.,* **118**(8), 083903, doi:10.1063/1.4929634.

Day, R., Fuller, M. & Schmidt, V., 1977. Hysteresis properties of titanomagnetites: grain-size and compositional dependence, *Phys. Earth planet. Inter.,* **13**(4), 260–267.

Dekkers, M.J., Mattéi, J.-L., Fillion, G. & Rochette, P., 1989. Grain-size dependence of the magnetic behavior of pyrrhotite during its low-temperature transition at 34 K, *Geophys. Res. Lett.,* **16**(8), 855–858.

Dekkers, M.J., 1988. Magnetic properties of natural pyrrhotite. Part I: Behaviour of initial susceptibility and saturation-magnetization-related rock-magnetic parameters in a grain-size dependent framework, *Phys. Earth planet. Inter.,* **52**(3–4), 376–393.

Dekkers, M.J., 1989. Magnetic properties of natural pyrrhotite. II. High- and low-temperature behaviour of Jrs and TRM as function of grain size, *Phys. Earth planet. Inter.,* **57**(3–4), 266–283.

Dunlop, D.J., 2003. Stepwise and continuous low-temperature demagnetization, *Geophys. Res. Lett.,* **30**(11), 1–4.

Dunlop, D.J. & Özdemir, Ö., 1997. *Rock Magnetism: Fundamentals and Frontiers*, Vol. 3, Cambridge Univ. Press.

Feinberg, J.M., Solheid, P.A., Swanson-Hysell, N.L., Jackson, M.J. & Bowles, J.A., 2015. Full vector low-temperature magnetic measurements of geologic materials, *Geochem. Geophys. Geosyst.,* **16**(1), 301–314.

Fillion, G. & Rochette, P., 1988. The low temperature transition in monoclinic pyrrhotite, *J. Phys. Colloq.,* **49**(C8), C8-907–C8-908.

Gattacceca, J. & Rochette, P., 2004. Toward a robust normalized magnetic paleointensity method applied to meteorites, *Earth planet. Sci. Lett.,* **227** (3–4), 377–393.

Gilder, S.A., Egli, R., Hochleitner, R., Roud, S.C., Volk, M.W.R., Le Goff, M. & de Wit, M., 2011. Anatomy of a pressure-induced, ferromagnetic-to-paramagnetic transition in pyrrhotite: implications for the formation pressure of diamonds, *J. geophys. Res.,* **116**(B10), doi:10.1029/2011JB008292.

Halgedahl, S.L., 1998. Revisiting the Lowrie–Fuller test: alternating field demagnetization characteristics of single-domain through multidomain glass–ceramic magnetite, *Earth planet. Sci. Lett.,* **160**(3–4), 257–271.

Halgedahl, S.L. & Fuller, M.D., 1981. The dependence of magnetic domain structure upon magnetization state in polycrystalline pyrrhotite, *Phys. Earth planet. Inter.,* **26**(1–2), 93–97.

Hodych, J.P., 1991. Low-temperature demagnetization of saturation remanence in rocks bearing multidomain magnetite, *Phys. Earth planet. Inter.,* **66**(3–4), 144–152.

Kind, J., Garcia-Rubio, I., Charilaou, M., Nowaczyk, N.R., Loffler, J.F. & Gehring, A.U., 2013. Domain-wall dynamics in 4C pyrrhotite at low temperature, *Geophys. J. Int.,* **195**(1), 192–199.

Koulialias, D., Kind, J., Charilaou, M., Weidler, P.G., Loffler, J.F. & Gehring, A.U., 2016. Variable defect structures cause the magnetic low-temperature transition in natural monoclinic pyrrhotite, *Geophys. J. Int.,* **204**(2), 961–967.

Martin-Hernandez, F., Dekkers, M.J., Bominaar-Silkens, I.M.A. & Maan, J.C., 2008. Magnetic anisotropy behaviour of pyrrhotite as determined by low- and high-field experiments, *Geophys. J. Int.,* **174**(1), 42–54.

Menyeh, A. & O'Reilly, W., 1997. Magnetic hysteresis properties of fine particles of monoclinic pyrrhotite Fe_7S_8, *J. Geomag. Geoelectr.,* **49**(7), 965–976.

Mikami, I., Hirone, T., Watanabe, H., Maeda, S., Adachi, K. & Yamada, M., 1959. On the magnetic anisotropy of a pyrrhotite crystal, *J. Phys. Soc. Japan,* **14**(11), 1568–1572.

Morimoto, N., Nakazawa, H., Nishigucmi, K. & Tokonami, M., 1970. Pyrrhotites: stoichiometric compounds with composition $Fe_{n-1}S_n$ ($n \geq 8$), *Science,* **168**(3934), 964–966.

Néel, M.L., 1952. Antiferromagnetism and ferrimagnetism, *Proc. Phys. Soc. A,* **65**(11), 869–885.

O'Reilly, W., 1984. *Rock and Mineral Magnetism,* Blackie & Son Ltd.

O'Reilly, W., Hoffmann, V., Chouker, A.C., Soffel, H.C. & Menyeh, A., 2000. Magnetic properties of synthetic analogues of pyrrhotite ore in the grain size range 1–24 m, *Geophys. J. Int.,* **142**(3), 669–683.

Pouchou, J.L. & Pichoir, F., 1984. New model for quantitative x-ray microanalysis. Part I: Application to the analysis of homogeneous samples, *Rech. Aerosp.,* **3,** 13–38.

Powell, A.V., Vaqueiro, P., Knight, K.S., Chapon, L.C. & Sánchez, R.D., 2004. Structure and magnetism in synthetic pyrrhotite Fe7S8: a powder neutron-diffraction study, *Phys. Rev. B,* **70**(1), 014415, doi:10.1103/PhysRevB.70.014415.

Pucher, R. & Fromm, K., 1985. Magnetkies—Ursache der magnetischen Anomalie Kirchzarten, in *Die Magnetische Anomalie Kirchzarten,* Vol. E23, pp. 263–277, ed. Homilius, J., Schweizerbart Science Publishers, Stuttgart, Germany.

Rochette, P. *et al.*, 2008. Magnetic classification of stony meteorites: 2. Non-ordinary chondrites, *Meteorit. Planet. Sci.,* **43**(5), 959–980.

Rochette, P., Fillion, G., Mattéi, J.-L. & Dekkers, M.J., 1990. Magnetic transition at 30–34 Kelvin in pyrrhotite: insight into a widespread occurrence of this mineral in rocks, *Earth planet. Sci. Lett.,* **98**(3–4), 319–328.

Rochette, P., Lorand, J.-P., Fillion, G. & Sautter, V., 2001. Pyrrhotite and the remanent magnetization of SNC meteorites: a changing perspective on Martian magnetism, *Earth planet. Sci. Lett.,* **190**(1–2), 1–12.

Rochette, P., Fillion, G. & Dekkers, M.J., 2011. Interpretation of low-temperature data. Part 4: The low-temperature magnetic transition of monoclinic pyrrhotite, *IRM Q,* **21**(1), 1–11.

Sato, K., Yamada, M. & Hirone, T., 1964. Megnetocrystalline anisotropy of pyrrhotite, *J. Phys. Soc. Japan,* **19**(9), 1592–1595.

Schwarz, E.J. & Vaughan, D.J., 1972. Magnetic phase relations of pyrrhotite, *J. Geomag. Geoelectr.,* **24**(4), 441–458.

Soffel, H.C., 1977. Pseudo-single-domain effects and single-domain multidomain transition in natural pyrrhotite deduced from domain structure observations, *J. Geophys.,* **42**(4), 351–359.

Soffel, H.C., 1981. Domain structure of natural fine-grained pyrrhotite in a rock matrix (diabase), *Phys. Earth planet. Inter.,* **26**(1–2), 98–106.

Tokonami, M., Nishiguchi, K. & Morimoto, N., 1972. Crystal structure of a monoclinic pyrrhotite (Fe7S8), *Am. Mineral.,* **57,** 1066–1080.

von Dobeneck, T., 1996. A systematic analysis of natural magnetic mineral assemblages based on modelling hysteresis loops with coercivity-related hyperbolic basis functions, *Geophys. J. Int.,* **124**(3), 675–694.

Weiss, B.P., Vali, H., Baudenbacher, F.J., Kirschvink, J.L., Stewart, S.T. & Shuster, D.L., 2002. Records of an ancient Martian magnetic field in ALH84001, *Earth planet. Sci. Lett.,* **201**(3–4), 449–463.

Weiss, B.P., Fong, L.E., Vali, H., Lima, E.A. & Baudenbacher, F.J., 2008. Paleointensity of the ancient Martian magnetic field, *Geophys. Res. Lett.,* **35**(23), L23207, doi:10.1029/2008GL035585.

Weiss, B.P., Gattacceca, J., Stanley, S., Rochette, P. & Christensen, U.R., 2009. Paleomagnetic records of meteorites and early planetesimal differentiation, *Space Sci. Rev.,* **152**(1–4), 341–390.

Wolfers, P., Fillion, G., Ouladdiaf, B., Ballou, R. & Rochette, P., 2011. The pyrrhotite 32 K magnetic transition, *Solid State Phenom.,* **170,** 174–179.